BLUNTNESS IMPACT ON DRAG AND LIFT OF FLAT-NOSE BODIES IN LOW-DENSITY HYPERSONIC FLIGHT

Wilson F. N. Santos
National Institute for Space Research
Combustion and Propulsion Laboratory
12630-000 Cachoeira Paulista, SP, Brazil
wilson@lcp.inpe.br

Abstract. *In this work the rarefied hypersonic flow past flat-nose leading edges is investigated by employing the Direct Simulation Monte Carlo (DSMC) method. A parametric study was carried out and the influences of the following parameters were investigated: (1) angle of attack and (2) Knudsen number, based on the frontal-face thickness, which covered from the transition flow regime to the free molecular flow one. The results demonstrate the sensitivity of drag, lift and lift-to-drag ratio to changes not only on the angle of attack but also on the frontal-face thickness of the leading edges. Comparisons based on drag, lift and lift-to-drag ratio are made between these blunt configurations and sharply pointed leading edges. Some significant differences between these shapes are noted on the aerodynamic surface quantities investigated. Of particular interest in this analysis is the aerodynamic performance of the leading edges defined by the lift-to-drag ratio, since blunt leading edges at incidence will allow leakage of the high-pressure lower surface flow into the upper surface region, causing a reduction in the lift. It was found that small frontal-face thickness, compared to the freestream mean free path, still has important effects on high Mach number leading edge flows. The analysis is of great importance since it is impossible to achieve ideally sharp leading edges of airframes, such as waveriders.*

Keywords*: Hypersonic Flow, DSMC, Blunt Leading Edge, Angle-of-attack, Lift-to-drag Ratio.*

1. INTRODUCTION

One of the main concerns of the aerodynamics of planetary entry is the heating rate and the damage that this may cause to the vehicle at hypersonic flight speed. The maximum heat flux to the structure usually occurs at the stagnation point of the vehicle. This maximum heat flux is inversely proportional to the square root of the nose radius of curvature. In this scenario, the use of blunt-nose shapes tends to alleviate the aerodynamic heating problem since the heat flux for blunt bodies is far lower than that for sharply pointed bodies. A round leading edge, with constant radius of curvature (circular cylinder) near the stagnation point, has usually been chosen. Nevertheless, shock detachment distance on a cylinder, with associated leakage, scales with the radius of curvature. In this fashion, shock wave will be detached from the leading edge and, hence, the aerodynamic performance — lift-to-drag (L/D) ratio — of the vehicle may be degraded from ideal performance, since the high-pressure gas from the lower surface may communicate with the gas on the upper surface.

Certain classes of non-circular shapes may provide the required bluntness with smaller shock separation than round leading edges, thus allowing manufacturing and heating control with reduced aerodynamic losses. According to Reller (1957), a method of designing low heat transfer bodies is devised on the premise that the rate of heat transfer to the nose will be low if the local velocity is low, while the rate of heat transfer to the afterbody will be low if the local density is low. A typical body that results from this design method consists of a flat nose followed by a highly curved, but for the most part slightly inclined, afterbody surface.

In this connection, flat-nose leading edges have been investigated (Santos, 2003, 2004a, 2004b, 2005, 2006 and 2007) as especially promising bluntness for hypersonic configurations in order to provide the leading-edge heating and manufacturing requirements. The investigations have focused on the low-density region in the upper atmosphere, where the non-equilibrium conditions are such that traditional CFD calculations are inappropriate to yield accurate results. In such a circumstance, the Direct Simulation Monte Carlo (DSMC) method has been employed to calculate the rarefied hypersonic flow on the flat-nose leading edges.

Santos (2003 and 2007) has investigated the sensitivity of the flowfield structure and the aerodynamic surface quantities to shape variations of such leading edges. The surface temperature effect on these flat-nose leading edges has been analyzed by Santos (2004a). In Santos (2004b), comparisons were made between flat-nose shapes and round shapes based on stagnation point heating and total drag. The analysis showed that round leading edges provide smaller stagnation point heating and larger total drag coefficient than flat-nose leading edges. In Santos (2005), a parametric study was performed on these flat-nose leading edges with a great deal of emphasis placed on the gas-surface interaction effects. It was instructive to explore the gas-surface interaction since as a space flight vehicle is exposed to a rarefied environment over a considerable time, a departure from the fully diffuse model is observed, resulting from the colliding molecules that clean the surface of the vehicle, which becomes gradually decontaminated. The flux distribution of scattered molecules emitted from clean surfaces frequently has a lobular shape that is centered about an

angle, which tends to approach the specular angle for very high energies and/or low angle of attack.

Finally, the compressibility effects on the flowfield structure of these flat-nose leading edges were computationally examined by Santos (2006).

The purpose of the present account is to extend further the previous analysis on flat-nose leading edges by investigating the impact of the angle of attack on the aerodynamic surface quantities. The knowledge of the aerodynamic surface properties at zero angle of attack is not sufficient to predict with certainty the flow characteristics over these shapes with incidence. Of particular interest in this analysis is the aerodynamic performance of the leading edges since blunt leading edges at incidence will allow leakage of the high-pressure from lower surface into the upper surface region, causing a reduction in the lift. In an effort to obtain further insight into the nature of the aerodynamic surface quantities of flat-nose leading edges under hypersonic transitional flow conditions, the essential characteristics of the angle of attack effect on heat transfer, drag, lift and drag-to-lift ratio will be examined for positive angle of attack with 5, 10, 15 and 20 degrees of incidence.

2. BODY SHAPE DEFINITION

The geometry of the leading edges considered in this work are the same as that presented in Santos (2003). The blunt shapes consist of a flat nose supplemented by an afterbody surface defined, in dimensionless form, by the following contour,

$$\bar{x} = \int_{\bar{y}=1}^{\bar{y}=\bar{y}_{\max}} \sqrt{\bar{y}^k - 1}\, d\bar{y} \qquad \text{where } \bar{x} = x/y_{nose} \text{ and } \bar{y} = y/y_{nose} \tag{1}$$

The flat-nose shapes are modeled by assuming a sharp leading edge of half angle θ with a circular cylinder of radius R inscribed tangent to the wedge. The flat-nose shapes, inscribed between the wedge and the cylinder, are also tangent to them at the same common point where they have the same slope angle. The circular cylinder diameter provides a reference for the amount of blunting desired on the leading edges. It was assumed a leading edge half angle of 10 degrees, a circular cylinder diameter of 10^{-2}m and flat-nose thickness t/λ_∞ of 0.01, 0.1 and 1, where $t = 2y_{nose}$ and λ_∞ is the freestream mean free path. Figure 1(a) illustrates this construction for the set of shapes investigated. From geometric considerations, the exponent k in Eq. (1) is obtained by matching slope on the wedge, circular cylinder and on the body shapes at the tangency point. For dimensionless thickness t/λ_∞ of 0.01, 0.1 and 1, the exponent k corresponds to 0.501, 0.746 and 1.465, respectively. The common body height H and the body length L are obtained in a straightforward manner. It was assumed that the leading edges are infinitely long but only the length L is considered, since the wake region behind the leading edges is not of interest in this investigation.

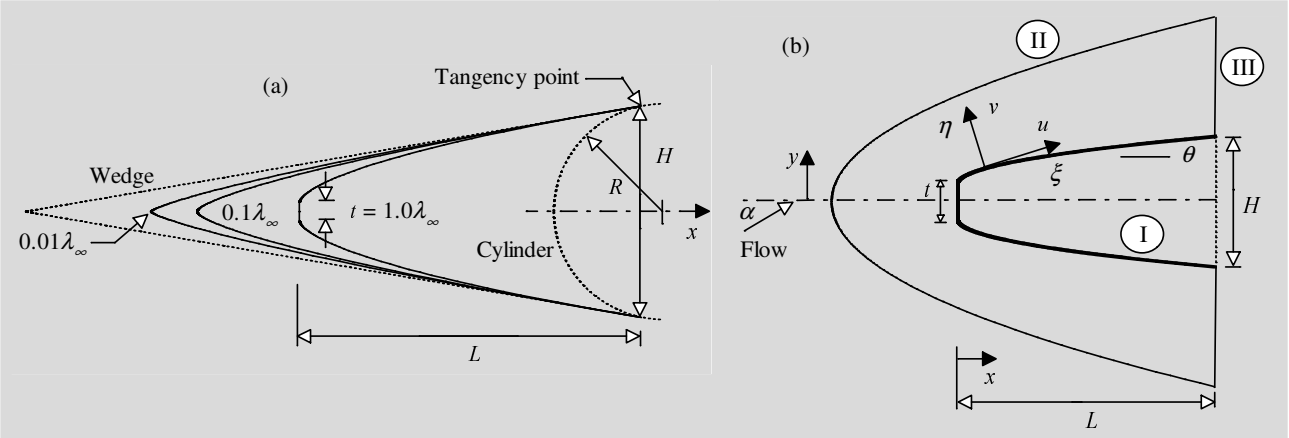

Figure 1: Drawing illustrating (a) the leading edge shapes and (b) the computational domain.

3. COMPUTATIONAL METHOD AND PROCEDURE

In order to study rarefied flow with a significant degree of non-equilibrium, the Direct Simulation Monte Carlo (DSMC) method (Bird, 1994) is usually employed. The DSMC method has become the most common computational technique for modeling complex transitional flows of engineering interest. The DSMC method model a gas flow by using a computer to track the trajectory of simulated particles, where each simulated particle represents a fixed number of real gas particles. The simulated particles are allowed to move and collide, while the computer stores their position coordinates, velocities and other physical properties such as internal energy.

In the present account, molecular collisions are modeled by the variable hard sphere (VHS) molecular model (bird, 1981) and by the no time counter (NTC) collision sampling technique (Bird, 1989). The mechanics of the energy exchange processes between kinetic and internal modes for rotation and vibration are controlled by the Borgnakke-Larsen statistical model (Borgnakke and Larsen, 1975). The essential feature of this model is that part of collisions is treated as completely inelastic, and the remainder of the molecular collisions is regarded as elastic. Simulations are performed using a non-reacting gas model consisting of two chemical species, N_2 and O_2. The vibrational temperature is controlled by the distribution of energy between the translational and rotational modes after an inelastic collision. The rates of rotational and vibrational relaxation are dictated by collision numbers Z_R and Z_V, respectively. The collision numbers are traditionally given as constants, 5 for rotation and 50 for vibration.

In order to implement the particle-particle collisions, the flowfield is divided into an arbitrary number of regions, which are subdivided into computational cells. The cells are further subdivided into four subcells, two subcells/cell in each direction. The cell provides a convenient reference sampling of the macroscopic gas properties, whereas the collision partners are selected from the same subcell for the establishment of the collision rate.

The computational domain used for the calculation is made large enough so that body disturbances do not reach the upstream and side boundaries, where freestream conditions are specified. A schematic view of the computational domain is depicted in Fig. 1(b). Side I is defined by the body surface. Diffuse reflection with complete surface thermal accommodation is the condition applied to this side. Side II is the freestream side through which simulated molecules enter and exit. Finally, the flow at the downstream outflow boundary, side III, is predominantly supersonic and vacuum condition is specified (Bird, 1994). At this boundary, simulated molecules can only exit.

The freestream and flow conditions used in the present calculations are those given by Santos (2003) and summarized in Tab. 1 and Tab. 2, respectively. The freestream velocity V_∞, assumed to be constant at 3.56 km/s, corresponds to freestream Mach number M_∞ of 12. The translational and vibrational temperatures in the freestream are in equilibrium at 220 K, and the leading edge surface has a constant temperature T_w of 880 K for all cases considered.

Table 1: Freestream Conditions

Temperature T_∞ (K)	Pressure p_∞ (N/m^2)	Density ρ_∞ (kg/m^3)	Number density n_∞ (m^{-3})	Viscosity μ_∞ (Ns/m^2)	Mean free path λ_∞ (m)	Velocity V_∞ (m/s)
220.0	5.582	8.753×10^{-5}	1.8209×10^{21}	1.455×10^{-5}	9.03×10^{-4}	3560

Table 2: Gas Properties

	Mole fraction X	Molecular mass m (kg)	Molecular diameter d (m)	Viscosity index ω
O_2	0.237	5.312×10^{-26}	4.01×10^{-10}	0.77
N_2	0.763	4.65×10^{-26}	4.11×10^{-10}	0.74

The overall Knudsen number Kn_t, defined as the ratio of the freestream mean free path λ_∞ to the leading edge thickness t, corresponds to 1, 10 and 100 for leading edge thickness t/λ_∞ of 1, 0.1 and 0.01, respectively. The Reynolds number Re_t covers the range from 0.193 to 19.3, based on conditions in the undisturbed stream with leading-edge thickness t as the characteristic length.

4. COMPUTATIONAL RESULTS AND DISCUSSION

This section focuses on the effects that take place on the aerodynamic surface quantities due to changes on the angle of attack as well as on the leading-edge shape. Aerodynamic surface quantities of particular interest in the transitional flow regime are number flux, heat transfer, wall pressure, wall shear stress, drag and lift. In this scenario, this section will discuss and compare differences of these quantities expressed in dimensionless coefficient form.

4.1. Number Flux

The number flux N is calculated by sampling the molecules impinging on the surface by unit time and unit area. A flux is regarded as positive if it is directed toward the body surface. The dependence of the number flux on the angle of attack α is illustrated in Figs. 2 and 3 for thickness Knudsen numbers Kn_t of 100 and 1, respectively, which correspond to leading-edge thickness t/λ_∞ of 0.01, and 1, respectively. In this set of plots, the dimensionless number flux N_f stands for the number flux N normalized by $n_\infty V_\infty$, where n_∞ is the freestream number density and V_∞ is the freestream velocity. In addition, S is the arc length s along the body surface, measured from the stagnation point, normalized by the freestream mean free path λ_∞. Also, FF stands for the half thickness of the frontal face of the leading edge. The number

flux distributions for the leading edge case represented by Kn_t of 10 are similar to those for the Kn_t of 100 and, in this case, they will no be shown.

Referring to Figs. 2(a) and 2(b), which correspond, respectively, the number flux distributions on the windward and leeward sides of the body surface, it is observed that the number flux roughly presents a constant value along the frontal face for the angle of attack range investigated. In contrast, by comparing to the zero-degree angle of attack case, the number flux decreases along the leeward side, due to the flow expansion, and it increases along the windward side of the leading edge, due to the flow compression. This is an expected behavior for positive angle of attack.

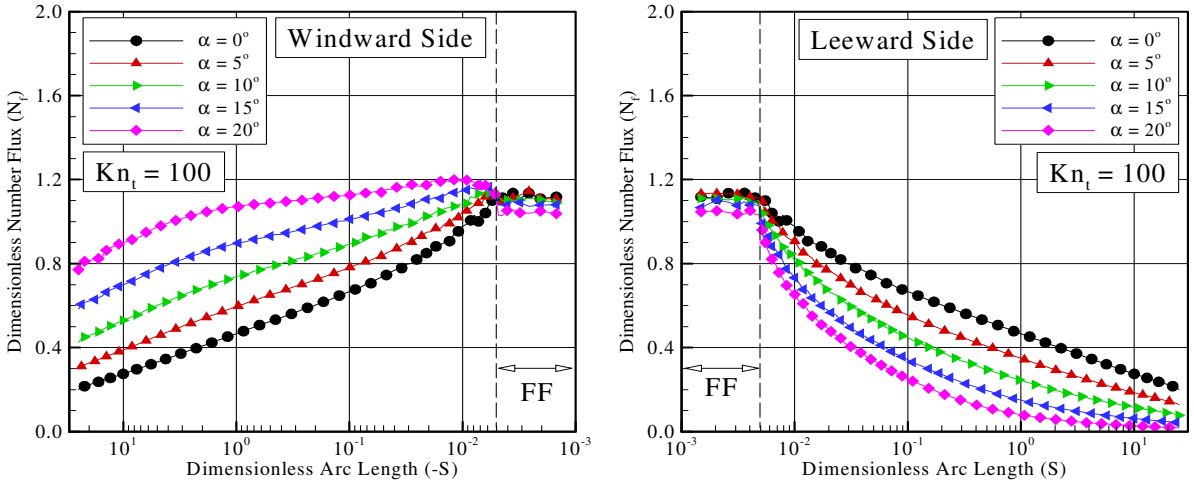

Figure 2: Distributions of the dimensionless number flux N_f along the (a) windward side and (b) leeward side as a function of the angle of attack for thickness Knudsen number Kn_t of 100.

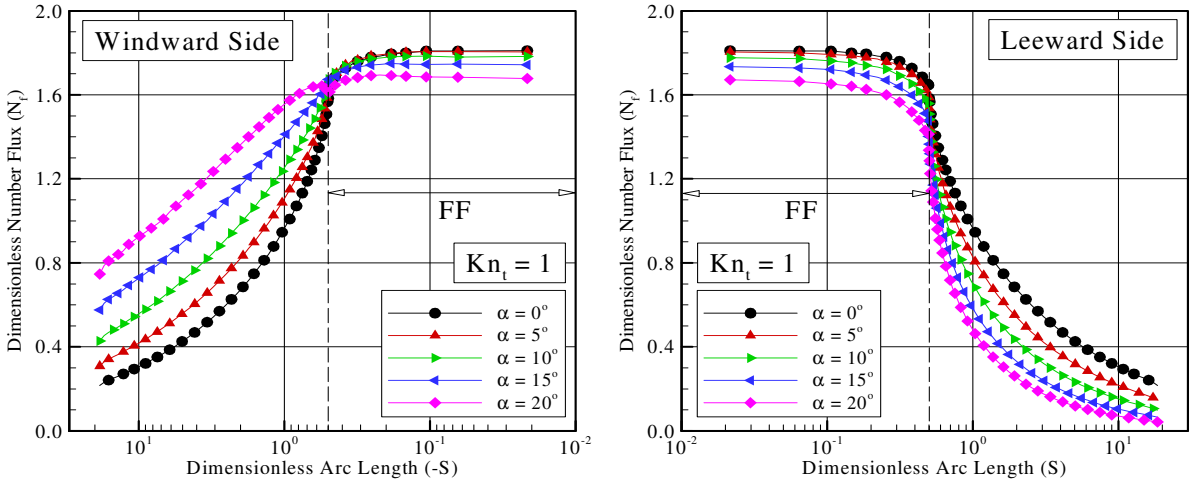

Figure 3: Distributions of the dimensionless number flux N_f along the (a) windward side and (b) leeward side as a function of the angle of attack for thickness Knudsen number Kn_t of 1.

According to Figs. 3(a) and 3(b), for the zero-degree angle of incidence, it is noted that the number flux presents a constant high value along the first half of the frontal face and, then decreases up to the frontal-face/afterbody junction with decreasing the thickness Knudsen number Kn_t. After that, the number flux N_f drops off sharply along the afterbody surface, in contrast to the the Kn_t = 100 case. Therefore, number flux to the front surface relies on the nose thickness in that it increases with increasing the leading-edge nose thickness t. At least at first sight, this behavior may be related to the collisions of two groups of molecules; the molecules reflecting from the nose of the leading edge and the molecules oncoming from the freestream. The molecules that are reflected from the body surface, which have a lower kinetic energy interact with the oncoming freestream molecules, which have a higher kinetic energy. Thus, the surface-reflected molecules re-collide with the body surface, which produce an increase in the dimensionless number flux in this region. At positive angle of attack, the stagnation point moves to the windward side of the leading edge. As a result, the number flux decreases along the frontal face, and dramatically increases along the windward side and decreases along the leeward side, due to the flow compression and flow expansion around the leading edge.

4.2. Heat Transfer Coefficient

The heat flux q_w to the body surface is calculated by the net energy flux of the molecules impinging on the surface. The net heat flux q_w is related to the sum of the translational, rotational and vibrational energies of both incident and reflected molecules. The heat flux is normalized by $\frac{1}{2}\rho_\infty V_\infty^3$ and presented in terms of heat transfer coefficient C_h.

The heat flux q_w to the body surface was defined in terms of the incident and reflected flow properties, and based upon the gas-surface interaction model of fully accommodated, complete diffuse re-emission. The diffuse model assumes that the molecules are reflected equally in all directions, quite independently of their incident speed and direction. Due to the diffuse reflection model, the reflected thermal velocity of the molecules impinging on the surface is obtained from Maxwellian distribution that takes into account for the temperature of the body surface. In this fashion, as the wall temperature is the same for all the cases investigated, the number of molecules impinging on the surface plays the important role on the reflected contribution to the net heat flux to the body surface.

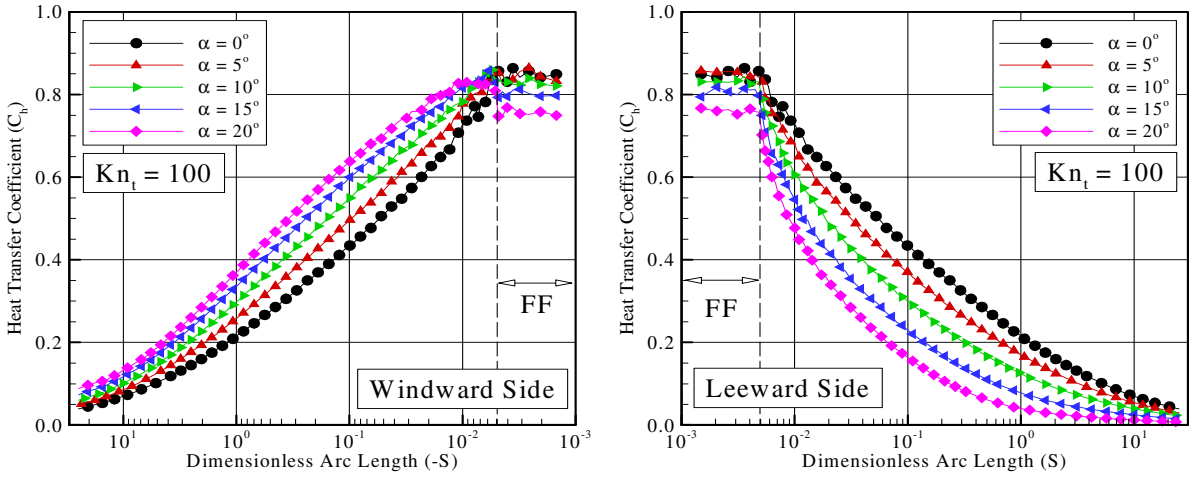

Figure 4: Distributions of heat transfer coefficient C_h along the (a) windward side and (b) leeward side as a function of the angle of attack for thickness Knudsen number Kn_t of 100.

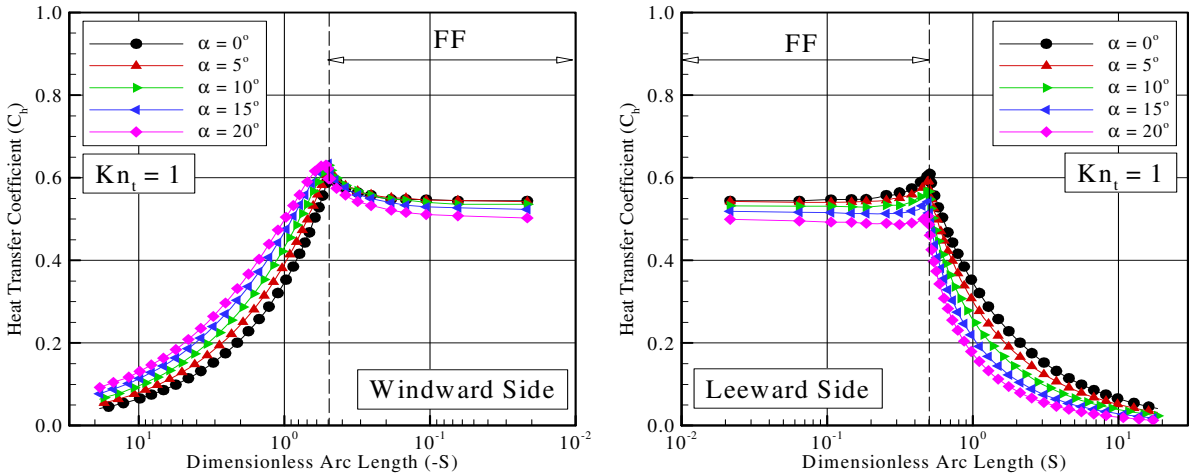

Figure 5: Distributions of heat transfer coefficient C_h along the (a) windward side and (b) leeward side as a function of the angle of attack for thickness Knudsen number Kn_t of 1.

The angle-of-attack effect, as well as the leading-edge thickness effect, on heat transfer coefficient C_h is illustrated in Figs. 4 and 5 for thickness Knudsen number Kn_t of 100 and 1, respectively. It is seen from these figures that the heat transfer coefficient C_h is sensitive not only to the frontal-face thickness but also to the angle of attack α. For zero-degree angle of incidence, the heat transfer coefficient C_h remains essentially constant along the frontal surface, and then it decreases sharply along the afterbody surface. Nevertheless, to the bluntest case investigated, Kn_t of 1, the heat transfer coefficient increases at the vicinity of the frontal-face/afterbody junction, in contrast to the sharpest case investigated, Kn_t of 100.

The stagnation region is generally considered as being the most thermally stressed zone in sharp/blunt bodies, as

shown by the Kn_t = 100 case. Nonetheless, as the frontal-face thickness increases, the most severe heat transfer region moves to the frontal-face/afterbody junction, as illustrated in Fig. 5. As the number of molecules impinging on the frontal surface decreases at the vicinity of the frontal-face/afterbody junction with the frontal-face thickness rise, as shown in Fig. 3, then the velocity of the molecules increases, as the flow approaches the frontal-face/afterbody junction, in order to increases the heat transfer coefficient. Moreover, the contribution of the translational energy to the net heat flux varies with the square of the velocity of the molecules. Therefore, the flatter the leading-edge nose is the lower the heat transfer coefficient at the stagnation point.

Referring to Figs. 4 and 5, it is clearly noticed that by increasing the angle of attack α causes the expected asymmetry in the heat transfer coefficient as the stagnation point moves from the symmetry axis to the frontal-face/afterbody junction on the windward side of the leading edges.

4.3. Pressure Coefficient

The pressure p_w on the body surface is calculated by the sum of the normal momentum fluxes of both incident and reflected molecules at each time step. Results are presented in terms of the pressure coefficient C_p.

Variations of the pressure coefficient C_p caused by changes on the angle of attack α and on the leading-edge thickness are demonstrated in Figs. 6 and 7 for thickness Knudsen number Kn_t of 100 and 1, respectively. As indeed is clear from this set of figures, at zero-degree angle of attack, the pressure coefficient follows the same trend presented by the number flux in that the pressure coefficient is high along the front surface, basically a constant value along it, and decreases dramatically along the afterbody surface at the vicinity of the frontal-face/afterbody junction.

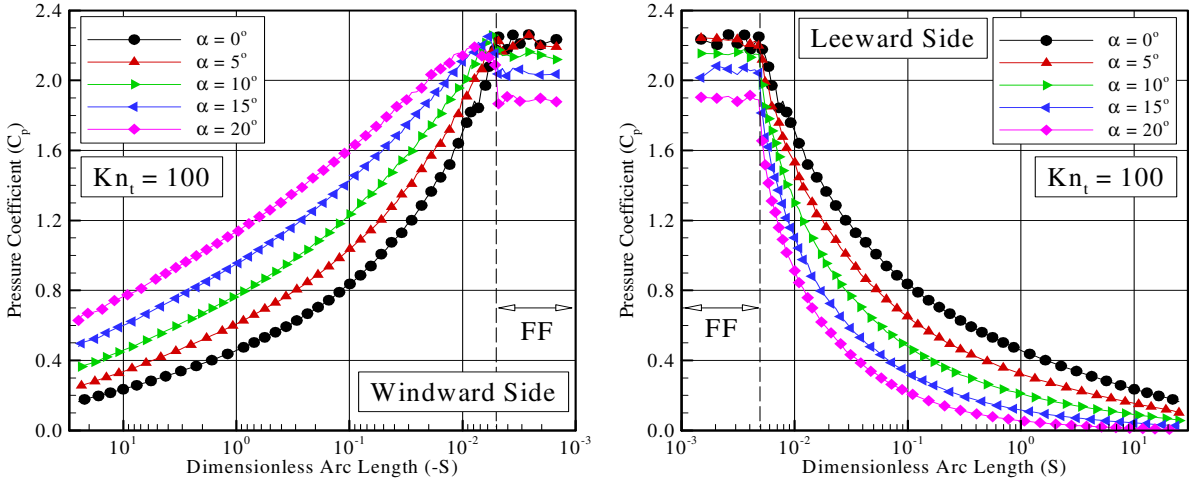

Figure 6: Distributions of pressure coefficient C_p along the (a) windward side and (b) leeward side as a function of the angle of attack for thickness Knudsen number Kn_t of 100.

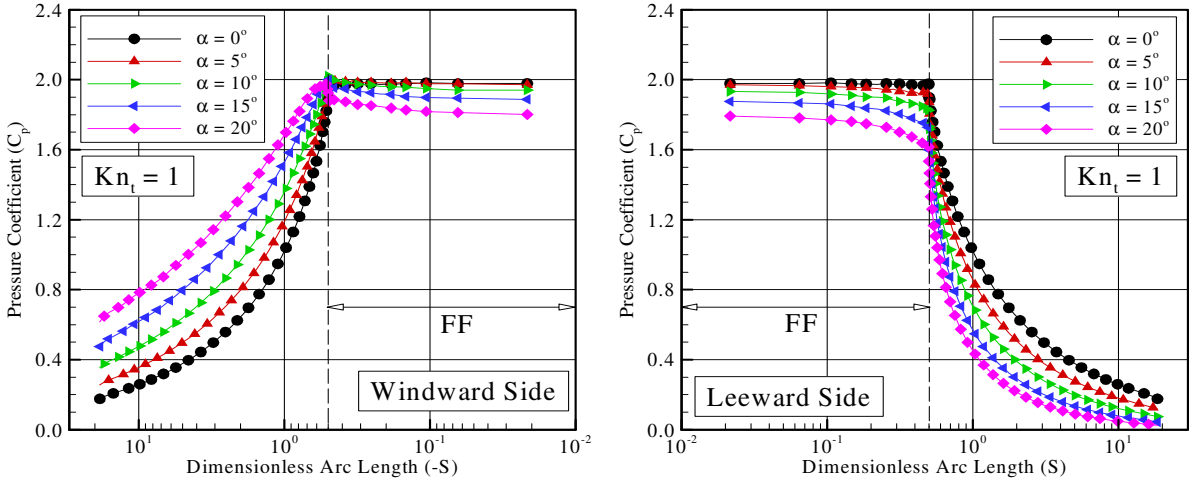

Figure 7: Distributions of pressure coefficient C_p along the (a) windward side and (b) leeward side as a function of the angle of attack for thickness Knudsen number Kn_t of 1.

It is very encouraging to observe that, at incidence, the normal momentum flux to the frontal face decreases and the tangential momentum flux increases, as will be seen subsequently. As a result, the pressure coefficient decreases, while the skin friction coefficient increases.

4.4. Skin Friction Coefficient

The shear stress τ_w on the body surface is calculated by averaging the tangential momentum transfer of the molecules impinging on the surface. For the diffuse reflection model imposed for the gas-surface interaction, reflected molecules have a tangential moment equal to zero, since the molecules essentially lose, on average, their tangential velocity component.

The shear stress τ_w on the body surface is normalized by $\frac{1}{2}\rho_\infty V_\infty^2$ and presented in terms of the dimensionless skin friction coefficient C_f. The influence of the angle of attack α and the leading-edge thickness on the skin friction coefficient is displayed in Figs. 8 and 9 for thickness Knudsen number Kn_t of 100 and 1, respectively.

According to these plots, at zero-degree angle of incidence, the skin friction coefficient C_f is zero at the stagnation point and slightly increases along the frontal surface up to the frontal-face/afterbody junction of the leading edge. After that, C_f increases significantly to a maximum value that depends on the frontal-face thickness, and then decreases downstream along the afterbody surface.

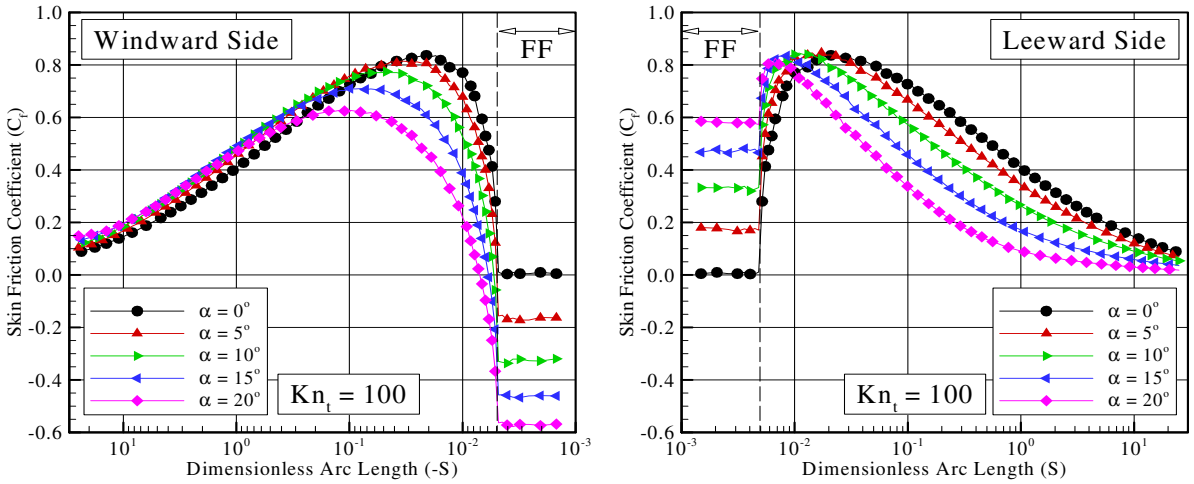

Figure 8: Distributions of skin friction coefficient C_f along the (a) windward side and (b) leeward side as a function of the angle of attack for thickness Knudsen number Kn_t of 100.

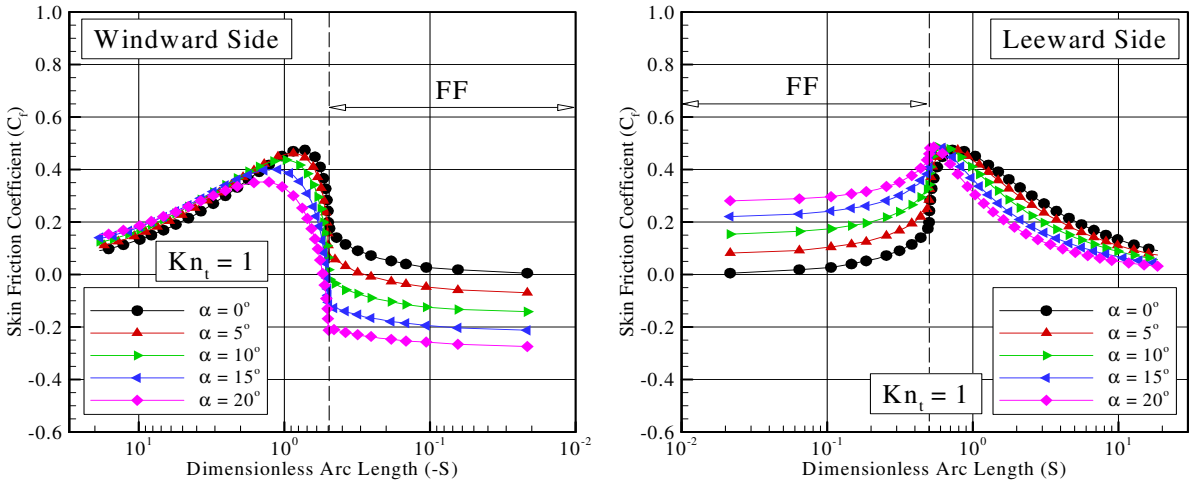

Figure 9: Distributions of skin friction coefficient C_f along the (a) windward side and (b) leeward side as a function of the angle of attack for thickness Knudsen number Kn_t of 1.

At incidence, a different behavior is noticed for the skin friction coefficient not only on the frontal surface but also on the afterbody surface. It is immediately evident from Figs. 8 and 9 that changes in the angle of attack α from 0 to 20

degrees produce substantial differences in the magnitude of the skin friction coefficient, particularly in a region of the afterbody surface that corresponds to a body-slope angle around 45 degrees (peak value). The direction of changes is toward larger skin friction coefficient at the vicinity of the frontal-face/afterbody junction on the leeward side and toward lower skin friction coefficient around the same station on the windward side of the afterbody surface. It may be recognized from these plots that the skin friction coefficient C_f is essentially negative along the frontal face on the windward side for angle of attack $\alpha > 0$ degree. It means that the force due to the shear stress is in the opposite direction as compared to that acting on the afterbody surface along the windward side of the afterbody surface.

4.5. Total Drag Coefficient

The drag on a surface in a gas flow results from the interchange of momentum between the surface and the molecules colliding with the surface. The total drag is obtained by the integration of the pressure p_w and shear stress τ_w distributions along the windward and leeward sides in the freestream direction. This corresponds from the symmetry axis of the leading edge to the tangent point common to all the leading edges (see Fig. 1). It is important to mention that the values for the total drag were obtained by assuming the shapes acting as leading edges. Therefore, no base pressure effects were taken into account on the calculations. Results for total drag are normalized by $\frac{1}{2}\rho_\infty V_\infty^2 H$ and presented as total drag coefficient C_d and its components of pressure drag coefficient C_{pd} and the skin friction drag coefficient C_{fd}.

The angle-of-attack effect on total drag coefficient C_d is demonstrated in Figs. 10(a-c) for thickness Knudsen number Kn_t of 100, 10 and 1, respectively. In this set of diagrams, the contributions of the pressure drag C_{pd} and the skin friction drag C_{fd} to the total drag C_d are compared to those for the "sharp-edged" wedge (see Fig. 1(a)). In this fashion, filled symbols stand for the wedge and empty symbols for the flat-nose leading edges.

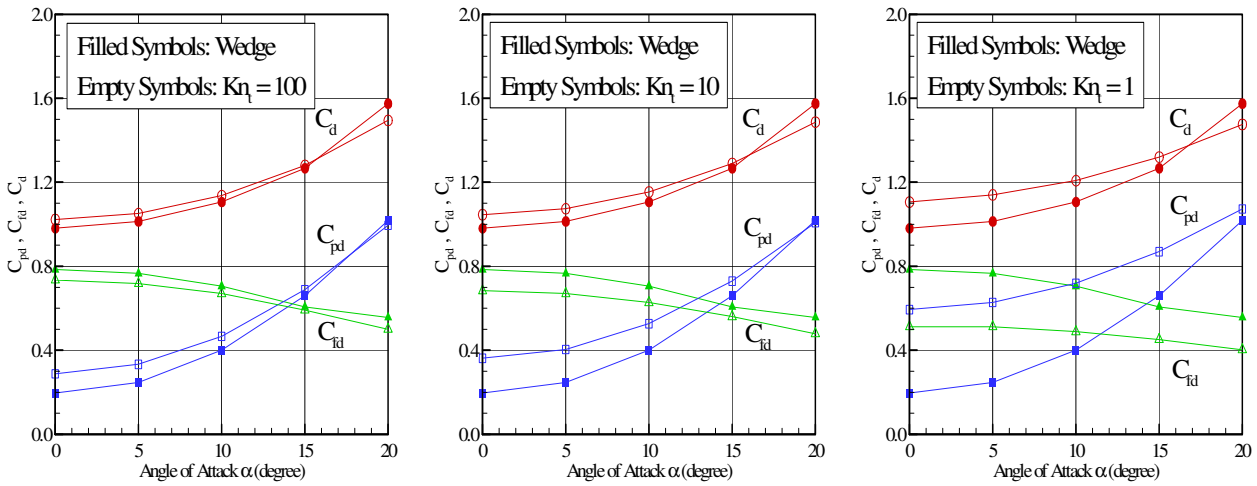

Figure 10: Pressure drag C_{pd}, skin friction drag C_{fd} and total drag C_d coefficients as a function of the angle of attack for thickness Knudsen number Kn_t of (a) 100, (b) 10 and (c) 1.

According to Figs. 10(a-c), at zero-degree angle of incidence, it is seen that as the leading edge becomes flatter, by decreasing the thickness Knudsen number Kn_t, the contribution of the pressure drag C_{pd} to the total drag increases and the contribution of the skin friction drag C_{fd} decreases. Although the net effect on total drag coefficient C_d depends on these to opposite behaviors, appreciable changes are observed in the total drag coefficient for the frontal-face thickness investigated, since C_{pd} and C_{fd} present different rate of changes. Nevertheless, the major contribution to the total drag coefficient C_d is attributed to the skin friction coefficient C_{fd}.

Still referring to Figs. 10(a-c), it is recognized that, at incidence, the contribution of the pressure drag C_{pd} to the total drag also increases and the contribution of the skin friction drag C_{fd} decreases. The reason for that is because the leading edges become "blunter" as seen from the freestream with the angle-of-attack rise. Of particular interest is the behavior of C_{pd} and C_{fd} for angle of attack $\alpha \geq 15$ degrees. For this range of incidence, the contribution of the pressure drag C_{pd} is higher than the skin friction drag contribution C_{fd}. Also of great significance is the particular case of $\alpha = 20$ degrees. For this angle of incidence, the total drag coefficient for the wedge is higher that that presented for the flat-nose leading edges.

4.6. Total Lift Coefficient

The lift force is obtained by the integration of the pressure p_w and shear stress τ_w distributions, along the windward and leeward sides, perpendicular to the freestream direction. This corresponds from the symmetry axis of the leading

edge to the tangent point common to all the leading edges (see Fig. 1). Similar to the drag coefficient, results for total lift are normalized by $\frac{1}{2}\rho_\infty V_\infty^2 H$ and presented as total lift coefficient C_l and its components of pressure lift coefficient C_{pl} and the skin friction lift coefficient C_{fl}.

The extent of changes on total lift coefficient C_l due to variations on the angle of attack α is illustrated in Figs. 11(a-c) for thickness Knudsen number Kn_t of 100, 10 and 1, respectively. In this set of figures, the contributions of the pressure lift C_{pl} and the skin friction lift C_{fl} to the total lift C_l are compared to those for the "sharp-edged" wedge. Again, filled symbols stand for the wedge and empty symbols for the flat-nose leading edges.

According to Figs. 11(a-c), it is noticed that the total lift C_l presents an expressive rise with increasing the angle of attack α dictated by the contribution of the pressure lift C_{pl}. In contrast, the contribution of the skin friction C_{fl} is in the sense of reducing the total lift C_l. Based on these figures, it is firmly established that the total lift C_l is dramatically reduced by a frontal-face thickness rise as compared to the sharp-edged wedge. It should also be mentioned in this context that, as the leading edge becomes flatter (by increasing thickness t), the shock wave standoff distance increases, and the high-pressure flow from the lower surface may communicate with the flow on the upper surface, resulting in a reduction in the lift coefficient.

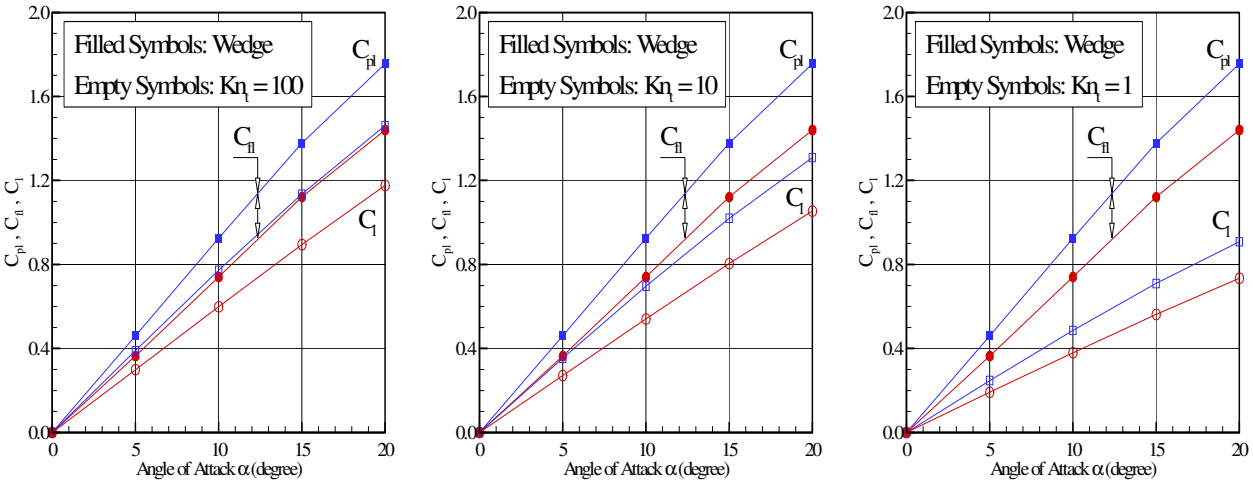

Figure 11: Pressure lift C_{pl}, skin friction lift C_{fl} and total lift C_l coefficients as a function of the angle of attack for thickness Knudsen number Kn_t of (a) 100, (b) 10 and (c) 1.

4.7. Lift-to-Drag (L/D) Ratio

Of particular interest in the present account is the aerodynamic performance of the leading edges given by the L/D ratio. It is known that blunt leading edges at incidence will allow leakage of the high-pressure lower surface flow into the upper surface region. As a result, lift force decreases and, consequently, causes a reduction on the L/D ratio.

The impact of the angle-of-attack on the L/D ratio is illustrated in Fig. 12 for the flat-nose leading edges investigated. For comparison purpose, the L/D ratio for the sharp-edged wedge is also presented in this figure.

According to Fig. 12, it is clearly seen that the L/D ratio increases with the angle of attack. In addition, the L/D ratio for sharp leading edges is higher than that for blunt leading edges. As an illustrative example, for 5-degree angle of incidence, the L/D for the sharp-edged wedge is 1.26, 1.42 and 2.14 times than that for the flat-nose leading edges represented by Kn_t of 100, 10 and 1, respectively. As a base of comparison, for 20-degree angle of incidence the L/D ratio changes to 1.16, 1.29, 1.84 times than that for Kn_t of 100, 10 and 1, respectively.

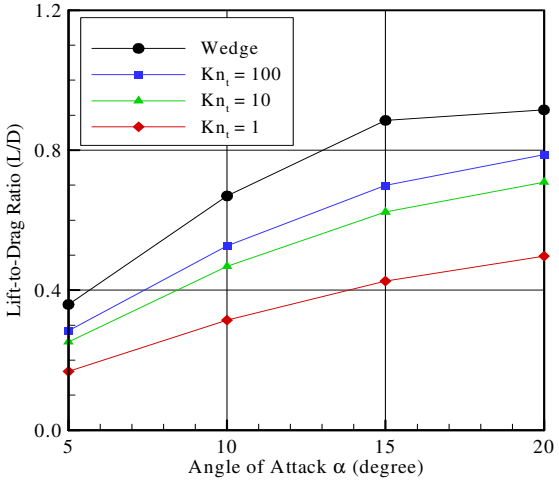

Figure 12: Comparison of the lift-to-drag ratio for flat-nose leading edge with that to sharp-edged wedge as a function of the angle of attack α.

5. CONCLUDING REMARKS

Computations of a rarefied hypersonic flow on sharp/blunt leading edges have been performed by using the Direct Simulation Monte Carlo method. The calculations provided information concerning the nature of the aerodynamic surface quantities for a family of truncated wedges.

Positive angle-of-attack effects on number flux, pressure, skin friction, heat transfer, drag and lift coefficients were investigated for a wide range of parameters. The incidence ranged from 0 to 20 degrees. In addition, the leading-edge nose thickness ranged from 0.01 to 1 of the freestream mean free path, corresponding thickness Knudsen numbers from 100 to 1. Cases considered in this study covered the hypersonic flow from the transitional flow regime to the free molecular flow regime.

The analysis showed that, at zero-degree angle of incidence, the peak value for the heat transfer coefficient is attained along the frontal face for the sharpest leading edge investigated. Conversely, for the bluntest leading-edge case investigated, the peak value moves to the frontal-face/afterbody junction. At positive angle of incidence, the peak value for the heat transfer coefficient is attained at the frontal-face/afterbody junction on the windward side of the leading edges. Also, the total drag coefficient slightly increased by increasing the frontal-face of the leading edge. Nevertheless, a significant increase in the total drag coefficient was observed by increasing the angle of attack. In addition, it was found that the lift coefficient decreased by increasing the frontal-face of the leading edges, since the leading edges changed from sharp to blunt one.

6. REFERENCES

Bird, G. A., 1981, "Monte Carlo Simulation in an Engineering Context", Progress in Astronautics and Aeronautics: Rarefied gas Dynamics, Ed. Sam S. Fisher, Vol. 74, part I, AIAA New York, pp. 239-255.

Bird, G. A., 1989, "Perception of Numerical Method in Rarefied Gasdynamics", Rarefied gas Dynamics: Theoretical and Computational Techniques, Eds. E. P. Muntz, and D. P. Weaver and D. H. Capbell, Vol. 118, Progress in Astronautics and Aeronautics, AIAA, New York, pp. 374-395.

Bird, G. A., 1994, "Molecular Gas Dynamics and the Direct Simulation of Gas Flows", Oxford University Press, Oxford, England, UK.

Borgnakke, C. and Larsen, P. S., 1975, "Statistical Collision Model for Monte Carlo Simulation of Polyatomic Gas Mixture", Journal of Computational Physics, Vol. 18, No. 4, pp. 405-420.

Nonweiler, T. R. F., 1959, "Aerodynamic Problems of Manned Space Vehicles", Journal of the Royal Aeronautical Society, Vol. 63, No. 589, pp. 521-528.

Reller Jr., J. O., 1957, "Heat Transfer to Blunt Nose Shapes with Laminar Boundary Layers at High Supersonic Speeds", NACA RM-A57FO3a.

Santos, W. F. N., 2003, "Aerodynamic Heating on Blunt Nose Shapes in Rarefied Hypersonic Flow", Proceedings of the 17th International Congress of Mechanical Engineering COBEM 2003, 10-14 Nov, São Paulo, SP, Brazil.

Santos, W. F. N., 2004a, "Surface Temperature Effects in Low-Density Flow over Flat-Nose Bodies at Hypersonic Speed. Part II: Aerodynamic Surface Quantities", Proceedings of the 10th Brazilian Congress of Thermal Sciences and Engineering ENCIT 2004, 29 Nov – 3 Dec, Rio de Janeiro, RJ, Brazil.

Santos, W. F. N., 2004b, "A Numerical Study of Drag and Heat Transfer to Blunt Nose Shapes in Rarefied Hypersonic Flow", Proceedings of the 24th International Congress of the Aeronautical Sciences, ICAS 2004, 29 Aug – 3 Sept, Yokohama, Japan.

Santos, W. F. N., 2005, "Gas-Surface Impact on Flowfield Structure of Low-Density Hypersonic Flow over Flat-Nose Bodies", Proceedings of the 18th International Congress of Mechanical Engineering COBEM 2005, 6-11 Nov, Ouro Preto, MG, Brazil.

Santos, W. F. N., 2006, "Compressibility Effect on Aerodynamic Heating and Drag of Hypersonic Flow over Flat-Nose Leading Edges", Proceedings of the 11th Brazilian Congress of Thermal Sciences and Engineering ENCIT 2006, 5 – 8 Dec, Curitiba, PR, Brazil.

Santos, W. F. N., 2007, "Simulation of Blunt Leading Edge Aerothermodynamics in Rarefied Hypersonic Flow". Journal of the Society of Mechanical Sciences and Engineering, Vol. 29, No. 2, pp. 123-135.